Focal-Plane Image and Beam Quality Sensors
for Adaptive Optics

Marc Cohen[†], Gert Cauwenberghs[†],
Mikhail Vorontsov[‡] and Gary Carhart[‡]

[†]Johns Hopkins University, Dept. of Electrical and Computer Engineering
3400 North Charles Street, Baltimore, MD 21211
[‡]Army Research Laboratory, Intelligent Optics Laboratory, Adelphi, MD 20783

Abstract

Control of adaptive optical elements for real-time wavefront phase distortion compensation is a rapidly growing field of research and technology development. Wavefront correction is essential for reliable long distance, near-ground laser communication as well as for imaging extended objects over large distances. Crucial to adaptively correcting the wavefront is a performance metric that can be directly evaluated from the acquired image or received laser beam, to provide real-time feedback to the controller adapting the wavefront. Custom VLSI controllers and sensors are a good match to the requirements of high resolution, real-time adaptive optical systems. In this paper we introduce two VLSI focal-plane sensors that supply image and beam quality metrics to an adaptive controller that performs parallel perturbative stochastic gradient descent on a spatial phase modulator in the control loop. For imaging applications, we designed an image quality metric chip that reports the high spatial frequency energy content of the received image. For laser communications applications, we designed a beam variance metric chip that calculates the compactness of the transmitted or received beam as well as its centroid location. We present experimental results from both sensor chips and demonstrate the beam variance metric chip in the feedback loop of an adaptive optics laser receiver.

1. Introduction

As an optical wave travels through an optically inhomogeneous medium such as the Earth's atmosphere, differences in the index of refraction along the propagation path cause local variations in the speed of light, which lead to wavefront *phase distortions* or *aberrations*. Phase distortions in the optical path severely limit the performance of a large class of optical systems and adaptive real-time correction of an optical field's wavefront spatial shape is an important task for a variety of applications: astronomical observations from the Earth, ground-to-ground and ground-to-air laser communication and imaging, laser technology, microscopy, lithography and medical imaging. Technologies for high resolution wavefront shaping are becoming available in the form of microelectromechanical mirrors

(MEMS), liquid crystal spatial light modulators (LC SLM) and liquid crystal television (LC TV).

We have been developing VLSI systems for direct real-time control of these wavefront correctors [17, 16, 14]. Our adaptive optics VLSI controller (AdOpt) performs model-free optimization on a measured scalar performance metric. The optimization strategy we use is *parallel perturbative stochastic gradient descent* [5]. Model-free control is advantageous because firstly we need not derive nor solve computationally intractable models of time-varying atmospheric turbulence and secondly, the architecture of control system becomes independent of the intracies of the specific task. The metric could be anything that indicates system "quality" and is computed based on available wavefront information in real-time. Depending on the type of adaptive optical system, the performance metric might be intensity of radiation at the focus [11, 21], image sharpness [18, 13] or scattered field statistical moments [19].

In model-free optimization, system performance is limited mainly by the precision at which the metric is acquired [6]. Therefore a critical component in the stochastic control system for adaptive optics is the metric sensor which quantifies an index of optical quality in real-time.

In this paper we present two analog VLSI focal-plane sensors which compute "image quality" for imaging applications and "beam quality" for laser transmitter/receiver applications. Section 2 briefly reviews our VLSI adaptive optics controller so as to emphasize the context for quality metric sensors. In Section 3 we discuss previous work on image and beam quality metrics. Section 4 describes our VLSI implementation of an "image quality" metric sensor chip which computes the high spatial frequency energy content of an image and presents experimental results from the chip. In Section 5 we describe our VLSI implementation of a laser "beam quality" metric sensor chip which computes the variance of the beam's cross-section and present experimental results from the chip. Here we demonstrate the successful use of the "beam quality" metric chip in a closed-loop adaptive optics system. We make concluding remarks in Section 6.

2. VLSI Control for Adaptive Optics

Figure 1 schematizes our approach to real-time wavefront control. An aberrated wavefront passes through an adaptive phase correcting device (MEMS mirror or LC SLM) and is focused onto a VLSI focal-plane sensor. This sensor computes a scalar quality metric $J(\mathbf{u})$ which quantifies the "quality" of the received image or beam. $J(\mathbf{u})$ is a function of all N controllable elements $\mathbf{u}$ in the wavefront phase corrector and provides the feedback signal used by the adaptive optics VLSI controller (AdOpt).

The parallel perturbative stochastic gradient descent algorithm can be interpreted as follows: at every time-step k, the controller differentially perturbs each element of the wavefront corrector u_j by δu_j and the resulting change in the measured performance metric is computed:

$$\delta J^{(k)} = J\left(u_1^{(k)} + \delta u_1^{(k)}, \ldots, u_N^{(k)} + \delta u_N^{(k)}\right) - J\left(u_1^{(k)} - \delta u_1^{(k)}, \ldots, u_N^{(k)} - \delta u_N^{(k)}\right). \quad (1)$$

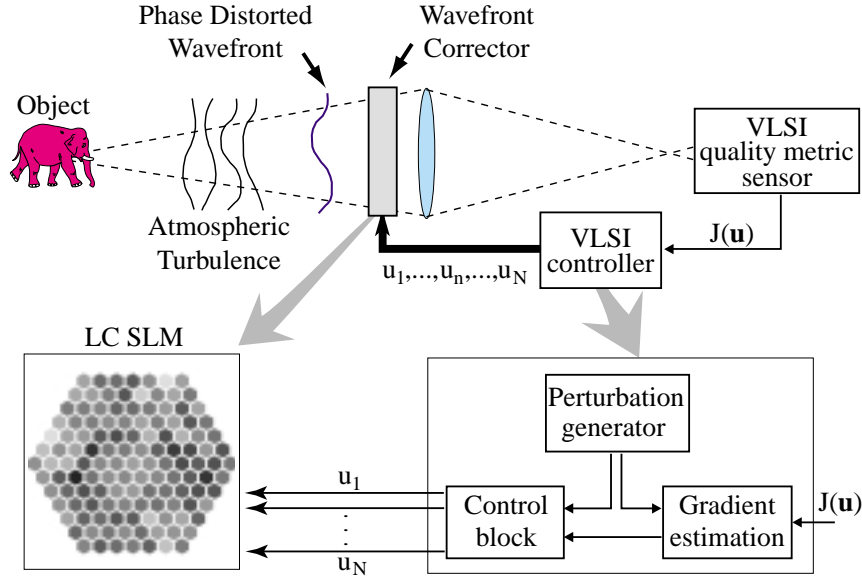Each of the control channels is updated in parallel at every time-step according to the

Figure 1. Adaptive optical system architecture. The VLSI quality metric sensor provides the feedback signal to the VLSI controller which directly controls all elements of the wavefront corrector in parallel.

following rule:

$$u_j^{(k+1)} = u_j^{(k)} - \gamma \delta J^{(k)} \delta u_j^{(k)} \tag{2}$$

where γ is a learning-rate parameter.

The fidelity of the closed loop system is strongly dependent on the chosen quality metric sensor which must compute $J(\mathbf{u})$ in real-time. In fact, reliable computation of $J(\mathbf{u})$ allows us to perform gradient descent in a large dimensional space without directly computing the gradient $(\partial J(\mathbf{u})/\partial \mathbf{u})$.

3. Performance Metrics

For model-free adaptive optics techniques an appropriate "oracle" of the system's performance must be specified and computed. This performance metric $J(\mathbf{u})$ must be carefully defined for the particular application and must be computable in a time much less than the characteristic time of the turbulence.

Several "sharpness" metrics have been suggested [18] and in particular, metrics for "image sharpness" and "focus" have been proposed [12] which take the form

$$J_{image} = \int_{\mathbf{r}} \| \nabla I\left(\mathbf{r}, t\right) \|^{\nu} d^2\mathbf{r} \,, \tag{3}$$

where ν is a parameter of the selected norm and $\mathbf{r} = \{x, y\}$ represents location in the image-plane. Delbrück [7, 8] has built VLSI implementations of (3) with $\nu = 1$ for computing image focus in real-time.

For laser beam focusing, metrics involve computing the sum over the image plane of functions of the two-dimensional beam intensity distribution $I(\mathbf{r}, t)$,

$$J_{beam} = \mathcal{F}_r \left\{ I\left(\mathbf{r}, t\right) \right\}. \tag{4}$$

where $\mathcal{F}$ represents some selected function. In the past, computing metrics of the form (4) has proven to be computationally too expensive for real-time applications. In response, Vorontsov *et.al.* [13] have suggested speckle field metrics based on the Fourier spectrum of $I(\mathbf{r}, t)$. The spectrum can be produced optically in real-time using Fourier optics and measured by a photo-detector. The authors have shown that this technique is essentially equivalent to metrics composed of sums of functions of intensity distributions.
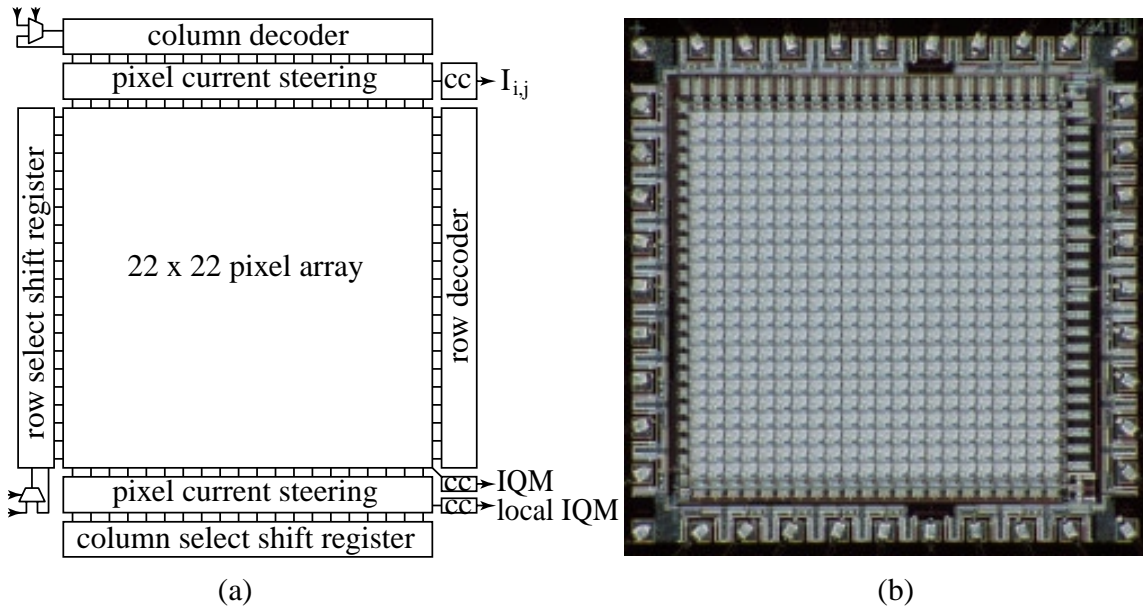

Figure 2. (a) IQM chip architecture. Row and column decoders allow random access to imager pixels. Row and column shift registers allow readout of user defined pixel groups for local image quality computation. Current steering circuits route the selected pixel currents to current conveyors (cc) which amplify the currents before sending them off-chip. (b) Photomicrograph of the 2.2×2.25 mm^2 IQM sensor chip manufactured through MOSIS in 1.2μm CMOS technology

Since we know how to design sophisticated VLSI image-plane processors to compute sums of functions of intensity distributions in real-time [15, 3, 7], we have the freedom to implement metrics designed specifically for each application. Our approach to quantifying the quality of a received image is to measure image sharpness in terms of the energy content at high spatial frequencies. Defocus of an image results in attenuation of the high spatial frequencies. We chose a simple measure of high spatial frequency energy keeping in mind our goal of VLSI implementation. Our image quality metric (IQM) is the intensity normalized sum of the absolute value of pixel photo-currents convolved with a

spatial high-pass filter,

$$\text{IQM} \;\;=\;\; \frac{1}{E}\sum_i \sum_j |I_{i,j} * K| \quad \text{with} \;\; K = \begin{bmatrix} 0 & -1 & 0 \\ -1 & 4 & -1 \\ 0 & -1 & 0 \end{bmatrix}, \tag{5}$$

where $I_{i,j}$ is the intensity at the $(i,j)^{th}$ pixel, and $E = \sum_i \sum_j I_{i,j}$ is the intensity of the received image.

For determining the quality of a transmitted or received laser beam, we define our beam variance metric (BVM) as the *variance* of the beam intensity distribution normalized by the square of the intensity,

$$\text{BVM} = \frac{N \cdot M \cdot}{E^2} \sum_i^N \sum_j^M I_{i,j}^2 \; , \tag{6}$$
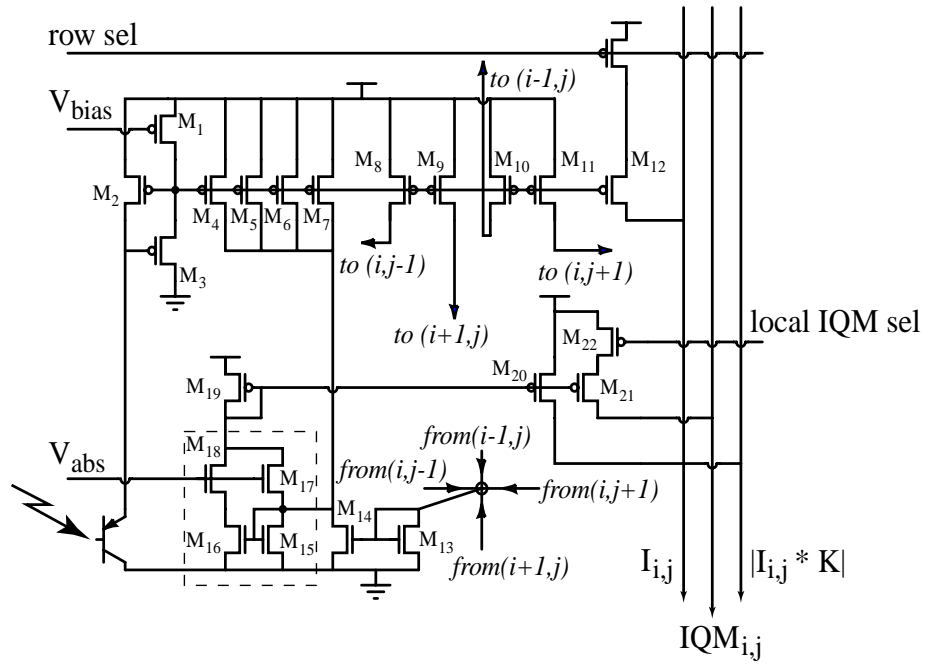
where N and M are the number of rows and columns respectively in the array of pixels. This metric is suitable for point sources and increases monotonically as the width of the focused beam decreases. We also compute the beam centroid in two dimensions, $\{X_C, Y_C\}$.
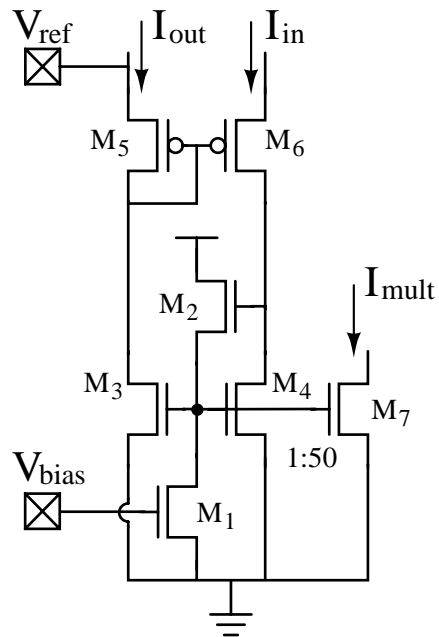
4. Image Quality Metric Chip

4.1. VLSI Implementation

We designed the IQM chip to produce several outputs: a captured image, global image quality as defined by (5) and local image quality (computed over a user defined group of pixels). The chip architecture is shown in Figure 2(a). It consists of a 22×22 array of pixels with perimeter pixels acting as dummy pixels to mitigate array edge-effects [1]. Random access readout of pixel currents is provided by row and column decoders at the periphery. Programmable row and column shift registers allow for readout of local image quality from a user-selected group of pixels. Multiplexers allow for either external loading of the shift registers or internal feedback. Local image quality is a performance metric used in synthetic imaging applications [4]. Current steering circuits route the selected pixel's or group of pixels' currents to current conveyors which amplify the currents before sending them off-chip for current-to-voltage conversion. Figure 2(b) shows a photomicrograph of the IQM sensor chip.

The pixel circuit diagram is shown in Figure 3(a). A vertical PNP bipolar transistor converts the collected photons into emitter photo-current $I_{i,j}$. Since nine copies of this current are needed, we use a current conveyor mirror (transistors M_1, M_2 and M_3) to set the gate voltage for current-copying transistors $M_8, \ldots, M_{12}$. The significant capacitive load from these nine transistor gates can be quickly charged/discharged by the current source M_1 whose gate voltage is a global value set off-chip. The convolution Kernel K described in (5) is formed as follows: $M_4, \ldots M_7$ source the central component of the Kernel, $+4I_{i,j}$ while M_{13} sinks current from the surrounding four pixels,

row sel

V_{bias} M_1

M_2

M_3

M_4 M_5 M_6 M_7 M_8 M_9 M_{10} M_{11} M_{12}

to (i-1,j)

to (i,j-1)

to (i,j+1)

to (i+1,j)

local IQM sel

M_{19}

M_{22}

M_{20} M_{21}

V_{abs}

M_{18}

M_{17}

from(i-1,j)

from(i,j-1)

from(i,j+1)

M_{16} M_{15} M_{14} M_{13}

from(i+1,j)

$I_{i,j}$ $|I_{i,j} * K|$

$IQM_{i,j}$

(a)

V_{ref} I_{out} I_{in}

M_5 M_6

M_2

I_{mult}

M_3 M_4 M_7

1:50

V_{bias}

M_1

(b)

Figure 3. (a) IQM Pixel circuit diagram and (b) Current Conveyor Current Mirror Schematic

$-I_{i+1,j}, -I_{i-1,j}, -I_{i,j+1}$ and $-I_{i,j-1}$. M_{13} mirrors this current through M_{14}. The difference between M_{14}'s drain current and the currents sourced by $M_4, \ldots, M_7$ is the current $I_{i,j} * K$. What remains is to compute the absolute value of this current. Transistors $M_{15}, \ldots, M_{18}$ shown in the dashed box make a simple current-mode absolute value circuit. If $I_{i,j} * K$ is positive, it is mirrored down the left side by M_{16} and sourced by diode-connected M_{19}. If negative, the current is directly sourced down the right side by M_{19}. M_{18} is a cascode for the mirror formed by M_{15} and M_{16}. Its gate voltage is a global bias signal set off-chip. M_{17} makes the absolute value circuit symmetric. The current through M_{19}, $|I_{i,j} * K|$ is mirrored by M_{20}. M_{20}'s drain is connected in common for all pixels in the array giving a total current of $\sum_i^N \sum_j^M |I_{i,j} * K|$. If the *local IQM sel* line (common for that row) is low, M_{22} is on, and M_{21} sources its current to the current steering circuits at the bottom periphery of the chip. The currents sourced by $M_8, \ldots, M_{12}$ are distributed to the neighboring four pixels, $I_{i+1,j}, I_{i-1,j}, I_{i,j+1}$ and $I_{i,j-1}$ for computing their own convolutions. The fabricated pixel measures $120\,\mu m$ on a side in a $1.2\mu m$ technology.

For readout of $I_{i,j}$, a 5 bit row decoder at the periphery selects the ith row and all pixels in that row send their currents $I_{i,j}$ for $j = 1, \ldots, 20$ to the current steering network at the top of the chip. A 5 bit column decoder selects the jth column and the selected pixel's current $I_{i,j}$ is steered to the periphery. The remaining unselected pixels' current in the selected i^{th} row are steered along a dummy line to the periphery. Both the selected and dummy lines are held at a fixed readout potential provided to the chip as a global bias voltage.
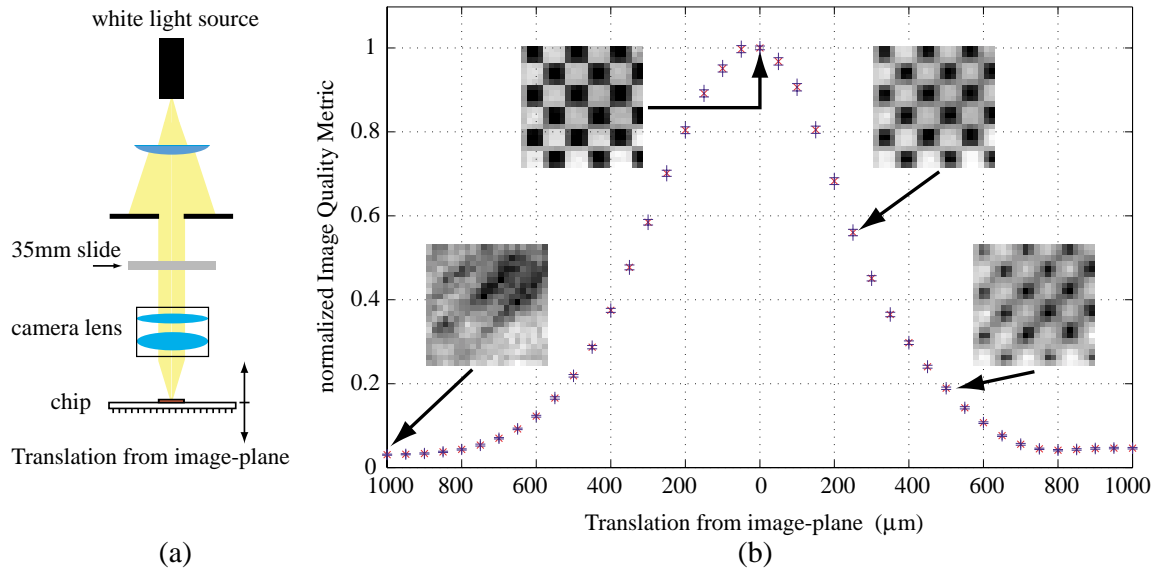

Figure 4. Bench-top testing of the Image Quality Metric chip. (a) Experimental setup and (b) Experimental Results

Readout of the local image quality metric is performed in a similar fashion. The programmable row and column shift registers take the place of the decoders. The row shift register selects a subset of rows in the array by pulling down the *local IQM sel* line. Currents from selected rows accumulate down the columns. Those columns that are selected

by the column shift register steer their currents to a common node which yields the local image quality for the selected subset of pixels. Those that are not selected steer their currents to a dummy line. Since the row and column shift registers can be individually clocked, the programmed grouping of pixels which contribute to the local image quality can be scanned across the chip. The current collection nodes are also held at a fixed potential. The currents $I_{i,j}$, IQM and local IQM are each sent to an on-chip CMOS current conveyor [20, 2] which clamps the voltage at which the current is read and further amplifies the current before it is sent off-chip. Figure 3(b) shows the circuit schematic for the CMOS current conveyor current mirror. Input current I_{in} enters the low impedance source of M_6. All four transistors $M_3, \ldots, M_6$ pass the same current so I_{out} is a copy of I_{in}. The source of M_3 is held at an externally set potential V_{ref} and an equal voltage appears at the source of M_6. M_1 and M_2 form a source follower so that M_4's gate voltage follows its drain voltage and passes current I_{in}. M_1's gate potential V_{bias} is set off-chip. The follower facilitates rapid charging and discharging of the large gate capacitance presented by transistors M_3, M_4 and M_7. The gained-up ($\approx 50\times$) output current I_{mult} is available at the high impedance drain of M_7.
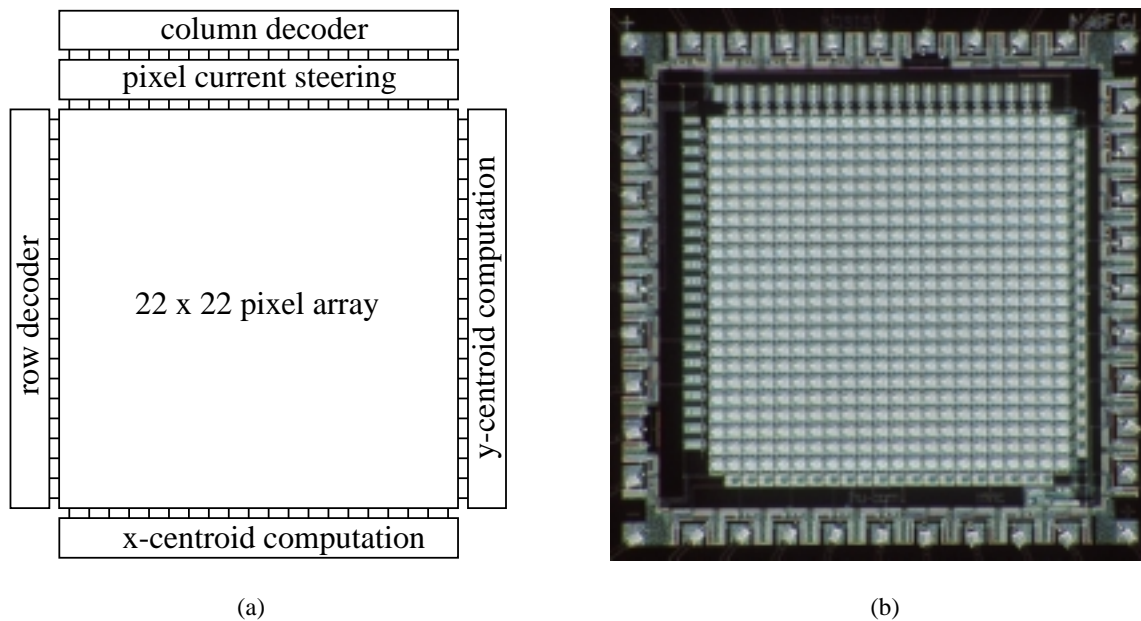

(a)

(b)

Figure 5. (a) BVM chip architecture. Row and column decoders provide random access readout of the 20×20 image. Current steering circuits route the selected pixel current off chip. x-and-y centroid circuits utilize pixel row and column sums at the periphery. (b) Photomicrograph of the 2.2×2.25mm^2 BVM sensor chip manufactured through MOSIS in 1.2μm CMOS technology

4.2. Experimental Results

We performed preliminary experiments on the Image Quality Metric sensor chip. Figure 4(a) shows our setup. A white light source was used to illuminate a gray-scale 35mm slide which was focused down onto the chip surface. The chip was mounted on a translation
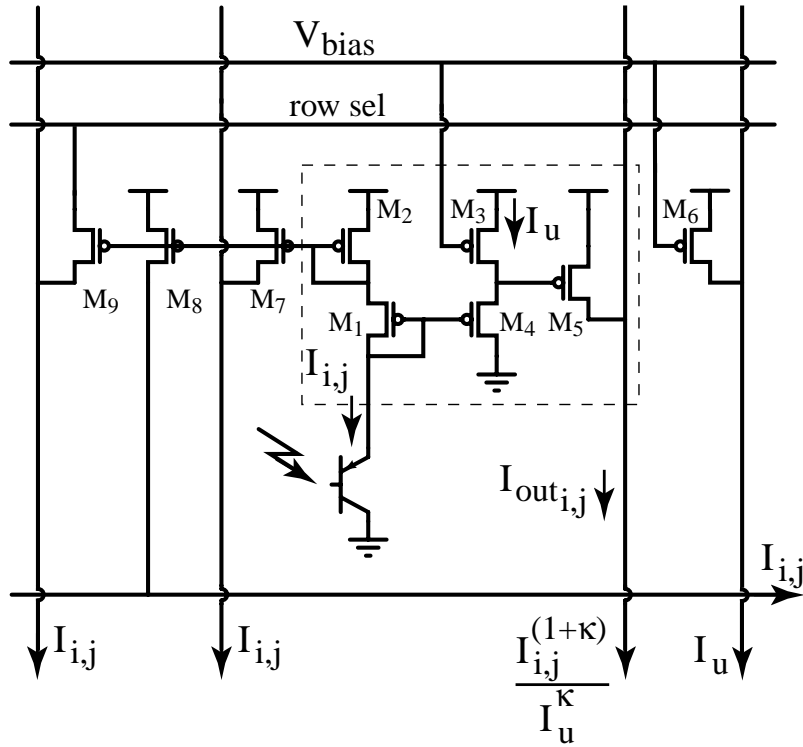
Figure 6. BVM pixel circuit diagram

stage so that it could be moved into-and-out-of the image plane. The 35mm slide consisted of a gray-scale checkerboard pattern. We moved the chip 1mm on either side of the image plane in steps of $50\mu m$. At each position we recorded the IQM computed by the chip and scanned the image captured by the chip. The results are plotted in Figure 4(b). We plot the measured normalized IQM as a function of displacement from the image plane along with ±3 std. dev. of the measured normalized IQM. We show four images scanned off the chip for various displacements from the image plane.

The results show desired properties of an image quality metric: namely, a high dynamic range of approximately 20; the largest value of IQM is obtained when the image is sharply focused on the chip; and the metric decreases monotonically away from this value for displacements on either side of the image plane.

5. Beam Variance Metric Chip

5.1. VLSI Implementation

We designed the BVM chip to image the focused laser beam, to compute the beam variance metric as described in (6) and to calculate the beam centroid. The chip's floorplan is shown in Figure 5(a).

Figure 6 shows the pixel circuit diagram. It consists of a 20×20 array of pixels surrounded by a ring of dummy pixels. Row and column decoders provide random access pixel current $I_{i,j}$ readout. Once a row has been selected, current steering circuits at the top
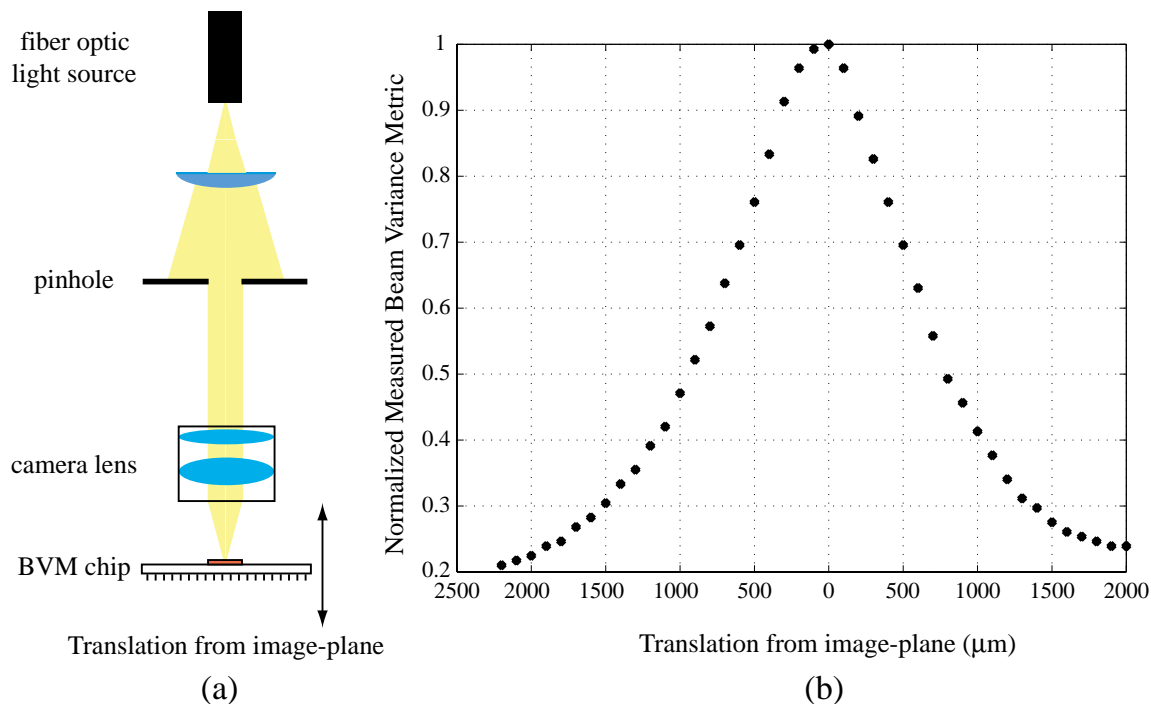
Figure 7. Bench-top testing of the Beam Variance Metric chip. (a) Experimental setup and (b) Experimental Results

of each column route the selected column's current to an output current line with all other non-selected column's currents routed to a dummy line. Both lines are held at the same fixed reference potential off-chip. Pixel row and column sums are continuously available for computing the beam's x-and-y centroid location $\{X_C, Y_c\}$ using DeWeerth and Mead's simple operational transconductance amplifier circuits [9]. These signals will be used to directly control tip-tilt mirrors. A photomicrograph of the BVM sensor chip is shown in Figure 5(b). Each pixel measures $70 \times 70 \mu m^2$ in a $1.2 \mu m$ technology. A vertical bipolar photo-transistor produces an emitter current $I_{i,j}$ proportional to the received photon energy. $I_{i,j}$ is copied by transistors M_7, M_8 and M_9. The first two copies are summed down columns and across rows respectively to form row and column sums at the periphery. M_9 sources $I_{i,j}$ to the current steering circuit at the top of the jth column only when its source is pulled high by the ith *row select* line. The *row select* line can be pulled slightly higher than the analog supply voltage to amplify the pixel current. The remaining transistors are used for computing the summands in (6). When operating in the sub-threshold regime, $M_1, \ldots, M_5$ form a translinear loop [10, 3] such that

$$I_{out_{i,j}} = \frac{I_{i,j} \, I_{i,j}^{\kappa}}{I_u^{\kappa}} \qquad (7)$$

where I_u is a sub-threshold bias current and $\kappa \approx 0.6$ is the sub-threshold slope factor for a pMOS transistor. [1] M_3 and M_6's gate voltages are globally connected and set off-chip.

---

[1]If transistors M_1 and M_4 were each in an n-well with their sources tied to their own well potential, κ would drop out of (7) to give $I_{out_{i,j}} \propto I_{i,j}^2$.

M_6 sources a copy of the bias current I_u which is globally summed to produce $N\,M\,I_u$ necessary for the correct current–domain form of (6),

$$BVM = \frac{N \cdot M \cdot I_u \sum_i^N \sum_j^M I_{i,j}^{(1+\kappa)}/I_u^{\kappa}}{\left(\sum_i^N \sum_j^M I_{i,j}\right)^2} \tag{8}$$
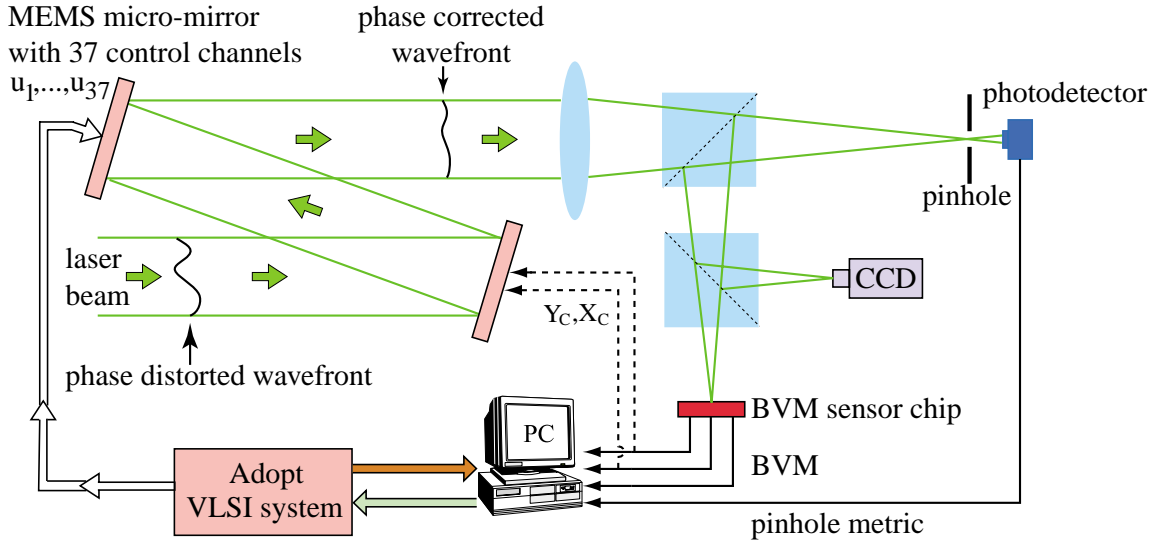

Figure 8. Experimental setup for verifying correct performance of the BVM sensor chip in a closed loop adaptive optics task

5.2. Experimental Results

We tested the beam variance metric chip using a similar setup to that used for testing the IQM sensor chip. The setup is shown in Figure 7(a).

The BVM chip was mounted on a translation stage which could be moved towards or away from the light source using a vernier. A fiber-optic white light source was focused down onto the chip surface which was positioned at the image plane. By moving the chip in front of and behind the image-plane we could defocus the beam thus distributing the light intensity over more pixels. We measured the beam variance metric as a function of the distance away from the image plane. Experimental results are shown in Figure 7(b). The measured BVM displays desirable properties for a quality metric: namely, it decays monotonically away from its maximum and exhibits a good dynamic range of approximately 5.

We also used the BVM sensor chip to provide the feedback signal $J\mathbf{u}$ in the closed loop adaptive optical setup shown in Figure 8. The beam from an Argon laser ($\lambda = 514\,\text{nm}$) was expanded to a diameter of 12 mm, reflected off a 2-degrees-of-freedom *x,y*-tilt mirror, and then reflected off a deformable membrane microelectromechanical mirror. The AdOpt system controlled all 37 elements of the MEMS mirror. A simple feedback signal used in adaptive optics experiments is the Strehl ratio of the focused beam. It is implemented with
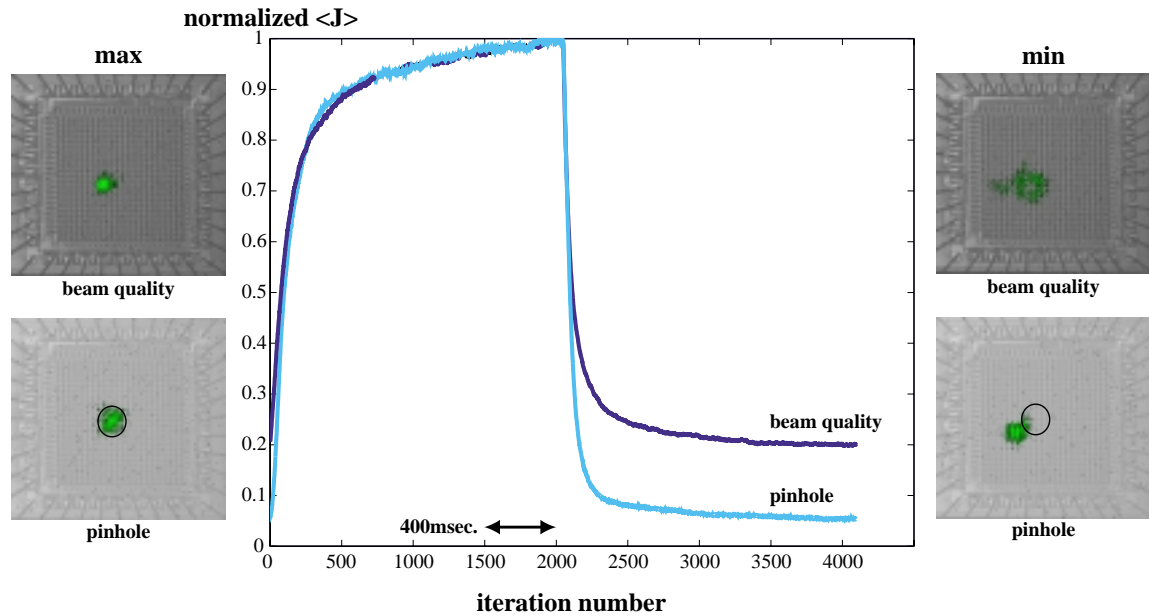
Figure 9. Experimental results comparing performance and shape of focused beam for *pinhole* **and** *beam variance* **metrics.**

a photo-detector which measures the intensity of the beam passing through a pinhole. When the beam's wavefront has been corrected, the compact beam passes most of its energy through the pinhole and the photo-detector registers a large output voltage. For comparison, both pinhole and BVM metrics were interfaced with a personal computer (PC). The PC supplies timing signals and bias voltages to the AdOpt VLSI system and also records and displays system performance in real-time.

We instructed the system to repeatedly maximize then minimize the performance metric and collected data from 100 such cycles using first the *pinhole metric* and then the *beam variance metric*. Figure 9 shows the results. We plot the normalized mean performance for both *pinhole* and *beam variance* metrics against iteration number for metric maximization followed by metric minimization. The *pinhole* metric produces a higher dynamic range than the *beam quality* metric. The CCD images to the left and right of this plot explain why. To the left we plot the imaged beam on the surface of the BVM chip for metric maximum and to the right for metric minimum. The position and relative size of the pinhole are marked for comparison on the chip image for the *pinhole* case. During metric maximization, the *beam variance* metric produces a compact circular beam (high output voltage) while during metric minimization, it produces a diffuse beam (low output voltage). The *pinhole* metric produces a less compact, elliptically shaped beam during maximization and for minimization simply steers the beam out of the pinhole (output voltage close to zero). For both metrics, maximization takes about 1 second while minimization takes about 0.5 seconds.

6. Conclusion

We adopted a model-free approach to real-time control of wavefront correctors for adaptive optics applications. Our model-free approach requires the computation of a scalar performance metric which is used as the feedback signal in the closed loop adaptive optical control system. This "oracle" of the system's performance can be tailored to the particular application. For imaging tasks, a measure of the high spatial frequency energy content of an image can be computed on the focal-plane in real-time. Our IQM sensor chip provides this performance metric for imaging applications. We described the design and successful bench-top testing of this IQM chip.

The energy distribution and centroid of a laser beam are important performance measures for laser transmitter and receiver tasks. Our BVM sensor chip successfully computes these quantities in real-time. We described the design and bench-top testing of this BVM chip. The BVM sensor was successfully used as the feedback sensor in our VLSI adaptive optics control system and yielded better performance than a conventional pinhole metric sensor.

Focal-plane VLSI performance sensors provide exciting new opportunities for adaptive optics applications. For some time now, adaptive optics has been unable to address many important application areas because of wavefront corrector and sensor limitations. High resolution wavefront control technology and performance sensor design, as discussed in this paper, are beginning to address these limitations. VLSI implementations offer the higher performance required for real-time high resolution adaptive optics applications, including high speed, small size, low power and low cost per control channel.

References

[1] A. Pavasovic, A.G. Andreou and C.R. Westgate. Characterization of subthreshold mos mismatch in transistors for vlsi systems. *Journal of VLSI Signal Processing*, 8:75–85, 1994.

[2] A.G. Andreou and K.A. Boahen. Synthetic neural circuits using current–domain signal representation. *Neural Computation*, 1:489–501, 1989.

[3] A.G. Andreou and K.A. Boahen. Translinear circuits in subthreshold mos. *Analog Integrated Circuits and Signal Processing*, 9:141–166, 1996.

[4] G.W. Carhart and M.A. Vorontsov. Synthetic imaging: nonadaptive anisoplanatic image correction in atmospheric turbulence. *Opt. Lett*, 23(10):745–747, 1998.

[5] G. Cauwenberghs. A fast stochastic error-descent algorithm for supervised learning and optimization. In *Advances in Neural Information Processing Systems, 5*, pages 244–251. Morgan Kaufman, San Mateo, CA, 1993.

[6] G. Cauwenberghs. Analog vlsi stochastic perturbative learning architectures. *J. Analog Integrated Circuits and Signal Processing*, 13(1-2):195–209, 1997.

[7] T. Delbrück. A chip that focuses an image on itself. In *Analog VLSI Implementation of Neural Systems*, pages 171–188. Kluwer Academic, 1989.

[8] T. Delbrück. Silicon retinas for autofocus. In *ISCAS 2000*, Geneva, May 2000.

[9] S.P. DeWeerth and C.A. Mead. A two-dimensional visual tracking array. In Jonathan Allen and F. Thomson Leighton, editors, *Advanced Research in VLSI, Proceedings of the Fifth MIT Conference*, pages 259–275. MIT Press, 1988.

[10] B. Gilbert. Current-mode circuits from a translinear viewpoint: A tutorial. In F.J. Lidgey C. Touma-zou and D.G. Haigh, editors, *Analogue IC Design: the current-mode approach*, pages 11–91. Peter Peregrinus, Ltd., 1990.

[11] J.W. Hardy. Active optics: a new technology for the control of light. *Proc. IEEE*, 66:651–697, 1978.

[12] B. Horn. Focusing. *Massachusetts Institute of Technology. Artificial Intelligence Laboratory*, Artificial Intelligence Memo 160, 1968.

[13] M.A. Vorontsov, G.W. Carhart, D.V. Pruidze, J.C. Ricklin and D.G. Voelz. Image quality criteria for an adaptive imaging system based on statistical analysis of the speckle field. *J. Opt. Soc. Am. A*, 13(7):1456–1466, 1996.

[14] M.A. Vorontsov, G.W. Carhart, M. Cohen and G. Cauwenberghs. Adaptive optics based on analog parallel stochastic optimization: analysis and experimental demonstration. *J. Opt. Soc. Am. A*, 17(8), 2000.

[15] C.A. Mead. Adaptive retina. In Mead and Ismail, editors, *Analog VLSI Implementations of Neural Systems*. Kluwer Academic, 1989.

[16] M.H. Cohen, G. Cauwenberghs, M.A. Vorontsov and G.W. Carhart. Adaptive wavefront correction: a hybrid vlsi/optical system implementing parallel stochastic gradient descent. In *Proc. of SPIE EU-ROPTO*, Florence, Italy, 1999.

[17] M.H. Cohen, G. Cauwenberghs, R.T. Edwards, M.A. Vorontsov and G.W. Carhart. Adopt: Analog vlsi stochastic optimization for adaptive optics. In *Proc. of IJCNN*, Washington DC, 1999.

[18] R.A. Muller and A. Buffington. Real-time correction of atmospherically degraded telescope images through image sharpening. *J. Opt. Soc. Am*, 64(9):1200–1210, 1974.

[19] V.I. Polejaev and M.A. Vorontsov. Adaptive active imaging system based on radiation focusing for extended targets. Proc. SPIE (3126), 1997.

[20] K.C. Smith and A. Sedra. The current conveyor – a new circuit building block. *Proceedings of The IEEE*, pages 1368–1369, 1968.

[21] R.K. Tyson. *Principles of Adaptive Optics*. Academic Press, Boston, 1991.